The Annals of Applied Statistics
2017, Vol. 11, No. 1, 297–319
DOI: 10.1214/16-AOAS1004

FUNCTIONAL TIME SERIES MODELS FOR ULTRAFINE PARTICLE DISTRIBUTIONS[1]

BY HEIDI J. FISCHER*, QUNFANG ZHANG†, YIFANG ZHU†, AND ROBERT E. WEISS†

Kaiser Permanente Southern California and UCLA Fielding School of Public Health†*

We propose Bayesian functional mixed effect time series models to explain the impact of engine idling on ultrafine particle (UFP) counts inside school buses. UFPs are toxic to humans and school engines emit particles primarily in the UFP size range. As school buses idle at bus stops, UFPs penetrate into cabins through cracks, doors, and windows. Counts increase over time at a size dependent rate once the engine turns on. How UFP counts inside buses vary by particle size over time and under different idling conditions is not yet well understood. We model UFP counts at a given time using a mixed effect model with a cubic B-spline basis as a function of size. The log residual variance over size is modeled using a quadratic B-spline basis to account for heterogeneity in error across size bin, and errors are autoregressive over time. Model predictions are communicated graphically. These methods provide information needed to quantify UFP counts by size and possibly minimize UFP exposure in the future.

1. Introduction. Ultrafine particles (UFPs) are particulate matter with diameters less than 100 nm. UFPs' small size and large surface area allow them to penetrate the lung, enter the circulatory system, and deposit in the brain [Oberdorster et al. (2004), Samet et al. (2009)], and it has been suggested that they are more toxic to humans than larger particles [Alessandrini et al. (2006), Delfino, Sioutas and Malik (2005), Ferin et al. (1990), Frampton et al. (2006)]. Though more research must be done within the UFP fraction, the health effects of particles are linked to particle size which determines the region in the lung the particles deposit [Morawska et al. (2008)]. Children are more sensitive than adults to UFPs because their physiological and immunological systems are still developing [Bennett and Zeman (1998)].

In the U.S., roughly 25 million children ride school buses daily. About 90 percent of buses are diesel powered, emitting particles primarily in the UFP size range [EPA (2002, 2014)]. As school buses idle at bus stops, UFPs from diesel emissions penetrate into cabins through cracks, doors, and windows. This so-called

Received December 2014; revised November 2016.

[1]Supported in part by the Health Effects Institute's Walter A. Rosenblith New Investigator Award under contract 4764-FRA06-3107-5.

Key words and phrases. Bayesian statistics, hierarchical models, varying coefficient models, heteroskedasticity.

"self-pollution" increases the exposure to UFPs of children on board [Zhang et al. (2012)]. How UFP counts vary by particle size as school buses idle over time and under different idling conditions is not yet well understood.

In this paper, we reanalyze data collected by researchers measuring particle counts inside buses first with the engine off and then after the engine is turned on and idles. A Scanning Mobility Particle Sizer (SMPS) counted particles per cubic centimeter in 102 *size bins* that group particles by diameter ranging from the first size bin containing particles of the smallest diameters, 7.37–7.64 nm, to the last size bin containing sizes of 269.0–278.8 nm. The ordered collection of counts in these 102 size bins at a single point in time is called a *UFP size distribution*, even though (i) technically particles with diameters greater than 100 nm are too big to be UFPs and (ii) the counts are not a distribution in the statistical sense. Size bin widths are approximately equally spaced on a log scale, and so UFP size distributions have more bins for the smaller UFP particles of interest. UFP distributions were collected over time during multiple experiments, or *runs*, making the data multivariate longitudinal.

In previous work, size distributions were typically modeled over size bin and time via *modal methods* [Whitby (1978), Whitby et al. (1991)], which treat particle size distributions as a mixture of densities [Hussein et al. (2005), Whitby et al. (1991), Wraith et al. (2009, 2014)]. Modal methods standardize particle counts: only information about the relative composition of particle size bins is retained. In modeling vehicle emissions, understanding actual particle counts is crucial. Modal methods have also not accounted for residual error which, as mentioned in Ramsay and Silverman (2005), may not be constant across size bin. Other previous work modeling UFP size distributions include the methods in Zhang et al. (2012), who modeled UFP counts inside idling school buses over time using separate univariate longitudinal models for each particle size bin.

The UFP size distribution is a function observed, with noise, over time. The primary interest in the current application is to explain the variation in the size distribution function across time in response to scalar covariates. This data setting follows the same structure as the functional methods described in Morris (2015) and Ramsay and Silverman (2005).

To best match this data setting, we propose Bayesian longitudinal functional time series models to model the impact of engine idling on UFP counts inside school buses. Unlike modal methods, functional time-series methods allow for inference on particle counts while accounting for differences in residual variance across particle size bin. This is also an improvement on the methods in Zhang et al. (2012); as we expect neighboring bins to have similar counts, their univariate longitudinal approach does not fully utilize the information in the data. We model UFP size distributions at a given time with a cubic B-spline basis [de Boor (1978)] and allow counts to increase over time at a size bin dependent rate once the engine is turned on. Our approach is a varying coefficient model as in Hastie and Tibshirani (1993) or Lang and Brezger (2004). We explore alternate models for the engine-on increase.

UFP size distributions naturally change in shape throughout each day, but with steady meteorological and background traffic, conditions can remain fairly constant during short periods of time. Stable conditions before the engine turned on resulted in clustering of *baseline* UFP size distributions within run. Despite stable conditions, pertubations from minute to minute due to a distant passing car, SMPS measurement error, or other natural disturbance were also observed, leading to additional residual correlation over size. Functional mixed-effect models have been utilized many times in the literature to model nested functional data [Berhane and Molitor (2008), Goldsmith and Kitago (2013), Morris et al. (2003)] and are ideal for this application. Baseline random effect functions are modeled by run, and additional curve-to-curve UFP deviations are split into the sum of minute-to-minute random effect functions and autoregressive error over time. To account for possible differential error across particle size bins, the log residual variance over size bin is modeled using a quadratic B-spline basis.

Interest centers on how mean particle counts change after the engine turns on as a function of size bin. Researchers are also interested in the mode of particle size counts, the mode height, and how both evolve after the engine turns on. We provide summaries of how the mode and mode height evolve as the engine idles. Plots are presented to aid in the interpretation of model inferences and make model output interpretable to nonstatisticians. Graphs also aid in diagnosis of lack of fit and can help suggest model improvements.

In Section 2 we describe the dataset, Section 3 presents our model, and Section 4 gives results. Finally, Section 5 is discussion.

2. UFP size distributions inside buses. UFP size distribution measurements were collected inside the bus every 2 minutes, and the current analysis considers measurements taken during the time period between 15 minutes before the engine was turned on and 20 minutes afterward. A set of UFP size distributions collected over this time period defines one run, though a few runs are shorter than the defined time. For certain runs, measurements occurred at odd-numbered minutes, while for other runs measurements occurred at even numbers. Runs took place under one of two window positions: (1) all windows closed, although some windows could not be closed tightly; and (2) eight rear windows, four on each side, open 20 cm. There are 21 runs in this dataset: 12 for windows open and 9 for windows closed. The study was conducted over one month in an open space under stable meteorological conditions without nearby UFP emission sources. Daily wind speed, temperature, and relative humidity ranged from 2.5 to 3.6 m/s, 18.2 and 22.6°C, and 58 to 80 percent, respectively [Zhang et al. (2012)].

Figure 1 plots UFP size distributions over time for 3 sample runs. Figure 1(a), (d) represents one run, where Figure (a) plots UFP size distributions over time before engine-on and and Figure (d) plots distributions for the same run after the engine is turned on. Figure 1(b), (e) and (c), (f) are organized similarly. Time is measured in minutes from when the engine is turned on, meaning measurements

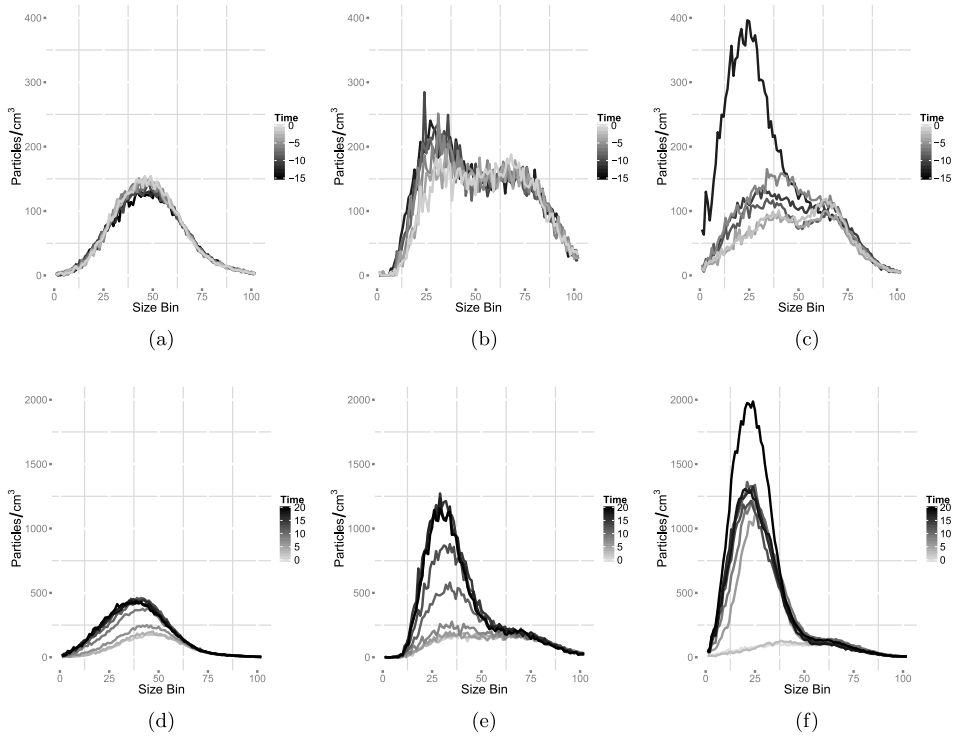

FIG. 1. *UFP size distributions over time for* 3 *sample runs. Figure* (a), (d) *represents one run, where Figure* (a) *plots UFP size distributions over time before engine-on and Figure* (d) *plots distributions for the same run after the engine is turned on. Figure* (b), (e) *and* (c), (f) *are organized similarly. Time is measured in minutes from when the engine is turned on, meaning measurements range from approximately* −15 *to* 20 *minutes and curves change color as time progresses. Figure* (a), (b), (c) *shows baseline UFP size distributions cluster within run, but minute-to-minute pertubations are present by curve to varying extents, in particular in Figure* 1(c), *which shows the effect of the rare occurrence of a passing vehicle in the fifteenth minute before engine-on. Figure* (d), (e), (f) *shows engine-on counts increase most in size bins smaller than* 60, *but suggests this increase varies by window position: in* (d) *the windows are closed, while in* (e), (f) *they are open. Figure* (f) *shows minute-to-minute pertubations can also be seen for engine-on, as counts rapidly increased in the* 20*th minute.*

range from approximately −15 to 20 minutes, and curves change color as time progresses. Figure 1(a), (b), (c) shows baseline UFP size distributions cluster within run, but minute-to-minute pertubations are present to varying extents, in particular, in Figure 1(c), which shows the effect of the rare occurence of a passing vehicle in the fifteenth minute before engine-on. Figure 1(d), (e), (f) shows engine-on counts increase most in size bins smaller than 60, but suggests this increase varies by window position: in (d) the windows are closed, while in (e), (f) they are open. Figure 1(f) shows minute-to-minute pertubations can also be seen for engine-on, as counts rapidly increase in the 20th minute.

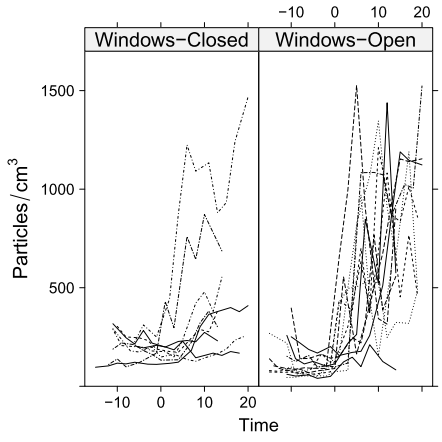

(a)

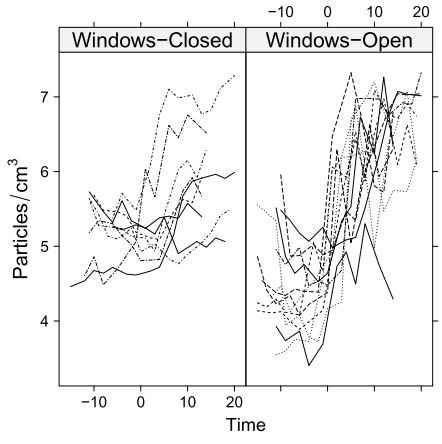

(b)

FIG. 2. *Figure* (a) *and* (b) *show particle counts and log particle counts over time, respectively, for size bin* 30 (20.9–21.7 *nm) for all runs by window position. Each line is a separate run. Counts for size bin* 30 *generally increase sharply when the engine first turns on, and then continue to increase at slower rates thereafter, though in some cases increases are not seen, particularly for the windows closed position. A log transformation allows for easier temporal modeling of counts.*

Figure 2(a) and (b) plot particle counts and log particle counts over time for size bin 30 (20.9–21.7 nm) for all runs by window position. Each line is a separate run. Counts for size bin 30 generally increase sharply when the engine first turns on, and then continue to increase at slower rates thereafter, though in some cases increases are not seen, particularly for the windows closed position. A log transformation allows for easier temporal modeling of counts [Whitby et al. (1991), Wraith et al. (2009, 2014)].

3. A time series semiparametric model for UFP size distributions. Let i be index run, where $i = 1, \ldots, R$ and for our data $R = 21$. Let s be index particle size bin, with $s = 1, \ldots, S$ and for our data $S = 102$. Time, t, has a run dependent range of $t_{\min,i}$ to $t_{\max,i}$. Time is measured in minutes and defined so that usually $t_{\min,i} = -14$ or -15, always the engine is turned on at $t = 0$, and usually $t_{\max,i} = 19$ or 20; there is modest variation by run for $t_{\min,i}$ and $t_{\max,i}$. Baseline refers to time before engine-on, when $t < 0$. Let $z(i)$ be an indicator of window position where $z(i) = 1$ corresponds to windows open and $z(i) = 0$ corresponds to windows closed. The window position should only affect measurements after $t = 0$, not before. Let $p(i, t)$ index each unique UFP distribution, where $p(i, t) = 1, \ldots, P$, and P is the total number of UFP distributions across all runs. We write $p \equiv p(i, t)$ and $z \equiv z(i)$ to simplify notation. Outcome y_{ist} is the natural log of particle count plus 10 for run i, size bin s at time t. A log transformation allows easier temporal modeling of counts.

3.1. *Modeling mean log counts.* Before engine-on, baseline mean log counts are expected to be constant over time and are modeled by a hierarchical model with random run intercepts which vary as a function of size bin s. At baseline, we expect y_{ist} to have a size bin specific population mean, α_s, and size bin specific random intercept, γ_{is}.

After engine-on, the y_{ist} increase additively from baseline levels. Let $\boldsymbol{f(t)}$ be a $J \times 1$ vector of functions of t, with jth element

$$f_j(t) = \begin{cases} 0, & t < 0, \\ m_j(t), & t \geq 0. \end{cases} \tag{3.1}$$

For a model with quadratic trend after engine-on, $J = 2, m_1(t) = t$, and $m_2(t) = t^2$. Other choices for $\boldsymbol{f(t)}$ are discussed in Section 3.3.

Engine-on increases in mean vary by window position z. Let $\boldsymbol{\delta_{zs}}$ be a $J \times 1$ vector of size bin and window position-specific regression coefficients for $\boldsymbol{f(t)}$. Then, for given s and z, the increase in mean log particle count from baseline is $\boldsymbol{\delta_{zs}^T f(t)}$.

The size-specific model for any time t is

$$y_{ist} = \alpha_s + \gamma_{is} + \boldsymbol{\delta_{zs}^T f(t)} + u_{ist}. \tag{3.2}$$

Errors u_{ist} are discussed shortly.

We want the baseline engine-off population mean α_s, baseline random intercept γ_{is}, and the coefficients for the time trends $\boldsymbol{\delta_{zs}}$ to vary smoothly by size bin s, and we model α_s, γ_{is}, and the elements of $\boldsymbol{\delta_{zs}}$ as cubic B-spline functions of s. Let $\boldsymbol{B(s)}$ be a cubic $(K \times 1)$ B-spline basis over size bin s with $(K - 4)$ knots. Let $\boldsymbol{\alpha}$ be the coefficients of $\boldsymbol{B(s)}$ for the population mean. Then

$$\alpha_s = \boldsymbol{\alpha^T B(s)},$$

and let $\boldsymbol{\gamma_i}$ be the coefficients of $\boldsymbol{B(s)}$ for random intercept for run i. Then

$$\gamma_{is} = \boldsymbol{\gamma_i^T B(s)}.$$

The vectors of random coefficients describing baseline UFP size distribution variation by run, $\boldsymbol{\gamma_i}$, have distribution

$$\boldsymbol{\gamma_i} | \boldsymbol{\Sigma_\gamma} \sim N_K(0, \boldsymbol{\Sigma_\gamma}) \tag{3.3}$$

for $i = 1, \ldots, R$. Together $\boldsymbol{\alpha^T B(s)} + \boldsymbol{\gamma_i^T B(s)}$ model the baseline UFP size distribution for run i and size bin s.

Let δ_{zsj} be the jth element of $\boldsymbol{\delta_{zs}}$. Set $\delta_{zsj} = \boldsymbol{\Delta_{zj}^T B(s)}$ so that δ_{zsj} varies smoothly over s according to coefficients in the $K \times 1$ vector $\boldsymbol{\Delta_{zj}}$. We define the $J \times K$ matrix $\boldsymbol{\Delta_z}$ so that $\boldsymbol{\Delta_{zj}}$ is the jth row of $\boldsymbol{\Delta_z}$. Then

$$\boldsymbol{f(t)}^T \boldsymbol{\Delta_z B(s)} = \boldsymbol{\delta_{zs}^T f(t)}. \tag{3.4}$$

There is one $\boldsymbol{\Delta_z}$, $J \times K$, for each window position, closed, $\boldsymbol{\Delta_0}$, and open, $\boldsymbol{\Delta_1}$.

3.2. *Modeling errors.* Errors u_{ist} are modeled in two parts. First, despite stable meteorological conditions, pertubations from minute to minute due to a passing car, SMPS measurement error, or other disturbance were observed, leading to a correlation of errors over size bin beyond that observed by run. We use the same cubic B-spline basis $\boldsymbol{B(s)}$ to model this correlation. Let $\boldsymbol{\nu_p}$ be the random perturbation coefficients of $\boldsymbol{B(s)}$ for UFP distribution p. These random vectors have distribution

$$\boldsymbol{\nu_p} | \boldsymbol{\Sigma_\nu} \sim N_K(0, \Sigma_\nu) \tag{3.5}$$

for $p = 1, \ldots, P$. To keep notation in terms of run, size, and time, we define $\xi_{ist} = \boldsymbol{\nu_p^T B(s)}$.

Because we have longitudinal data, we typically expect higher correlation in observations closer together in time and lower correlations between observations farther apart in time. This is the second part of our error, called v_{ist}, which we model with an autoregressive process over time conditioning on the first observation [Prado and West (2010)]:

$$v_{ist} = \theta v_{i,s,t-1} + \varepsilon_{ist}, \tag{3.6}$$

$$\varepsilon_{ist} \sim N\big(0, \sigma_s^2\big), \tag{3.7}$$

where the lag one correlation is θ, and σ_s^2 is the variance of ε_{ist} given $v_{i,s,t-1}$.

The error variance σ_s^2 may not be constant and needs to vary smoothly over size bin, matching the functional methods described in Ramsay and Silverman (2005). The log variance is modeled with a separate quadratic ($L \times 1$) B-spline basis over size bin, $\boldsymbol{B_{err}(s)}$, with $(L - 3)$ knots. Log variance is modeled

$$\log\big(\sigma_s^2\big) = \boldsymbol{\eta}^T \boldsymbol{B_{err}(s)} + w_s, \tag{3.8}$$

$$w_s \sim N\big(0, \tau_\eta^2\big), \tag{3.9}$$

where the w_s are small normal residual terms with known variance τ_η^2 added to $\boldsymbol{\eta}^T \boldsymbol{B}_{\mathbf{err}}(\boldsymbol{s})$ to enable efficient MCMC sampling [Baladandayuthapani, Mallick and Carroll (2005), Crainiceanu et al. (2007), Hadfield (2010)]. We set τ_η^2 to a small number to not add too much variation.

The two-part errors then are modeled as

$$u_{ist} = \xi_{ist} + v_{ist}, \tag{3.10}$$

along with equations (3.5), (3.6), (3.7), (3.8), and (3.9). Now we discuss time trend models after engine-on.

3.3. *Time trend models*. The time trend after the engine turns on has not been explored in current research, and thus we consider competing parametric models.

3.3.1. *Quadratic time trend*. For the model with quadratic trend, $J = 2$, $m_1(t) = t$, $m_2(t) = t^2$, and $\boldsymbol{\Delta}_z$ is a $2 \times K$ matrix with rows of coefficients of $\boldsymbol{B}(\boldsymbol{s})$ for the linear and quadratic time trend terms.

3.3.2. *Jump models with a quadratic time trend*. We consider an immediate jump in counts when the engine first turns on followed by a quadratic time trend. Here $J = 3$, $m_1(t) = 1$, $m_2(t) = t$, and $m_3(t) = t^2$.

3.4. *Random jumps for the time trend*. Finally, we considered random jumps as part of the time trend to determine if further improvements in model fit were possible. The random jump time trend uses the same B-spline basis $\boldsymbol{B}(\boldsymbol{s})$ to vary time trend coefficients by size bin. Let $\boldsymbol{g}(\boldsymbol{t})$ be a $G \times 1$ vector of functions of t, defined analogously to $\boldsymbol{f}(\boldsymbol{t})$ in equation (3.1). Let $\boldsymbol{\Upsilon_i}$ be defined as $\boldsymbol{\Delta}_z$ in equation (3.4), except $\boldsymbol{\Upsilon_i}$ varies by run, not window position, and $\boldsymbol{\Upsilon_i} | \boldsymbol{\Sigma_\Upsilon} \sim N(0, \boldsymbol{\Sigma_\Upsilon})$. A model with a random jump would have $\boldsymbol{g}(\boldsymbol{t}) = 1$, $G = 1$, and $\boldsymbol{\Upsilon_i}$ be a $K \times 1$ random vector. This notation allows for more complex random effects after engine-on, however, residual analysis did not indicate a need for additional random effects; see Appendix A [Fischer et al. (2017)], Figures A1, A2, and A3.

The model now takes the form

$$y_{ist} = \boldsymbol{\alpha}^T \boldsymbol{B}(\boldsymbol{s}) + \boldsymbol{\gamma_i}^T \boldsymbol{B}(\boldsymbol{s}) + \boldsymbol{f}(\boldsymbol{t})^T \boldsymbol{\Delta}_z \boldsymbol{B}(\boldsymbol{s}) + \boldsymbol{g}(\boldsymbol{t})^T \boldsymbol{\Upsilon_i} \boldsymbol{B}(\boldsymbol{s}) + u_{ist}, \tag{3.11}$$

along with equations in Section 3.2.

The model with only quadratic time trend is referred to as the *no-jump* model, while the model with an engine-on jump is referred to as the *jump* model. These models are described by equation (3.11) without the term $\boldsymbol{g}(\boldsymbol{t})^T \boldsymbol{\Upsilon_i} \boldsymbol{B}(\boldsymbol{s})$. The model with the engine-on random jump is referred to as the *random jump* model and is described by equation (3.11). We used 7 knots (implying $K = 11$) to choose between engine-on parametric forms, and then experimented with various values of K to determine which resulted in our preferred model fit.

3.5. *Priors*. Proper priors are used on all parameters. Priors for the fixed effects $\boldsymbol{\alpha}$ and $\boldsymbol{\Delta}_{zj}$, $j = 1, \ldots, J$, are

$$\boldsymbol{\alpha}|c_\alpha \sim N_K(\mathbf{4}, c_\alpha \mathbf{I}_K), \tag{3.12}$$

$$\boldsymbol{\Delta}_{zj}|c_{\delta_j} \sim N_K(\mathbf{0}, c_{\delta_j}\mathbf{I}_K), \tag{3.13}$$

where $\boldsymbol{I}_K$ is the $K \times K$ identity matrix. We believed the engine-off fixed effects would be between two and six on the log scale with fair uncertainty around that value, and thus we gave a prior mean equal to 4 and set c_α equal to 16. For the engine-on fixed effects we set the prior means to zero to match the null hypothesis of no engine-on effect for either window position. Because we do not believe this null hypothesis, we set the prior variances, c_{δ_j}, to be fairly large to accommodate the anticipated prior uncertainty. If jump, linear, and quadratic terms contribute equally to the engine-on effect at 10 minutes, the linear term should be about $1/10$ of the jump term, and the quadratic term should be about $1/100$ of the linear term. Thus, for jump models, we set $c_{\delta_1} = 2$, $c_{\delta_2} = 2/10$, and $c_{\delta_3} = 2/100$. The no-jump model removed the jump portion of the prior, $c_{\delta_1}\mathbf{I}_k$.

The prior for the correlation parameter θ is taken to be truncated normal, as it is conditionally conjugate up to a constant, which improves computational speed in an already complicated model

$$\theta|\mu_\theta, \sigma_\theta^2 \sim N\big(\mu_\theta, \sigma_\theta^2\big)\,\mathrm{I}\big[\theta \in (-1, 0.9)\big], \tag{3.14}$$

with the indicator function giving the lower -1 and upper 0.9 truncation points. The upper limit of 0.9 was chosen to avoid singularity in the likelihood, noted to be an issue in Palmer and Pettit (1996), and additionally because it is reasonable to believe that θ is much smaller than 0.9 though likely positive. We set $\mu_\theta = 0$ and $\sigma_\theta^2 = 0.1$ to allow some flexibility over this range. Covariance matrices $\boldsymbol{\Sigma}_{\boldsymbol{\gamma}}$, $\boldsymbol{\Sigma}_{\boldsymbol{v}}$, and $\boldsymbol{\Sigma}_{\boldsymbol{\Upsilon}}$ are given Inverse-Wishart priors

$$\boldsymbol{\Sigma}_{\boldsymbol{\gamma}} \sim \text{Inverse-Wishart}\big(f, (f - K - 1) * \boldsymbol{M}\big), \tag{3.15}$$

$$\boldsymbol{\Sigma}_{\boldsymbol{v}} \sim \text{Inverse-Wishart}(K + 1, \boldsymbol{D}), \tag{3.16}$$

$$\boldsymbol{\Sigma}_{\boldsymbol{\Upsilon}} \sim \text{Inverse-Wishart}(K + 1, 2\boldsymbol{D}), \tag{3.17}$$

where the known $K \times K$ scale matrix $\boldsymbol{M}$ uses information from 65 other engine-off experiments reported in Zhang et al. (2012) but not used in the current analysis: a Bayesian linear mixed-effects model using $\boldsymbol{B}(\boldsymbol{s})$ for the fixed and random UFP size distribution effects was run using log counts from this additional data. The estimated posterior covariance matrix for the random effects from this fit was used as the scale matrix $\boldsymbol{M}$ in the Inverse-Wishart prior, and we set $f = 65$. This allowed information available about typical correlations in UFP size distribution shapes from urban environments under similar meteorological conditions to be used, supplementing the sparse information available in the current dataset with only 21 runs.

There was no prior information available for $\boldsymbol{\Sigma_\nu}$ and $\boldsymbol{\Sigma_\Upsilon}$. We believed the variances would be smaller for minute-to-minute random effects than the engine-off random effects, but because we did not have information on this, to be conservative, we set the scale matrix $\boldsymbol{D}$ to be a diagonal matrix with the diagonal equal to twice the mean of all the variances in $\boldsymbol{M}$. We set the scale matrix for $\boldsymbol{\Sigma_\Upsilon}$ to $2\boldsymbol{D}$ to reflect larger possible variances for the random jump compared to minute-to-minute random effects. Both priors were given low degrees of freedom equal to $K + 1$.

The prior for the coefficients of the log variance is taken to be

$$\boldsymbol{\eta} \sim N_L\big(\log(0.4), g^2 \boldsymbol{I_L}\big), \tag{3.18}$$

where 0.4 was the mean residual error reported in the experiments of Zhang et al. (2012) not examined here, $\boldsymbol{I_L}$ is the $L \times L$ identity matrix, and the hyperparameter g is set to put a 95 probability around residual variances between 0.2 and 0.7. The prior is centered at a constant residual across size bins.

Sensitivity analyses were conducted; prior variances (or the mean of prior variances in the case of random effects) were halved and doubled to give two additional fits.

3.6. *Computing overview.* Posterior estimates are obtained via Markov Chain Monte Carlo (MCMC) simulations [Gelfand and Smith (1990), Hastings (1970)] using JAGS 3.3.0 [Plummer (2003)]. The MCMC convergence and mixing properties were assessed by visual inspection of the autocorrelation and chain histories of individual parameters, some of which are presented in Appendix A [Fischer et al. (2017)] in Figures A4 and A5. Convergence appeared to be immediate for all parameters. The orginal dataset, as well as R and JAGS code to conduct the main analyses and produce plots from the paper, is included in Appendix B [Fischer et al. (2017)].

3.7. *Estimates of interest.* Let $\boldsymbol{Y}$ be the vector of all y_{ist}. To investigate model fit, we plotted subsets of equation (3.11): baseline UFP size distributions, $\boldsymbol{\alpha^T B(s)} + \boldsymbol{\gamma_i^T B(s)}$, and engine-on posterior time trend changes, $\boldsymbol{f(t)^T \Delta_z B(s)}$. Integrating out random engine-off and engine-on effects, predicted mean log counts at size bin s and time t are $\psi_{st} = \boldsymbol{\alpha^T B(s)} + \boldsymbol{f(t)^T \Delta_z B(s)}$.

For emission monitoring purposes, posterior predictions must be transformed back to their original scale. Conditional on run i and UFP distribution p, engine-on predicted counts at size bin s have marginal variance, $\lambda_s^2 \equiv \operatorname{var}(y_{ist}|\boldsymbol{\gamma_i}, \boldsymbol{\nu_p}, \boldsymbol{\Upsilon_i})$ that is the same for all times t. Then $\operatorname{var}(v_{ist}|\boldsymbol{\gamma_i}, \boldsymbol{\nu_p}, \boldsymbol{\Upsilon_i}) = \operatorname{var}(\theta v_{i,s,t-1} + \varepsilon_{ist}|\boldsymbol{\gamma_i}, \boldsymbol{\nu_p}, \boldsymbol{\Upsilon_i})$ so that $\lambda_s^2 = \theta^2\lambda_s^2 + \sigma_s^2$ to give $\lambda_s^2 = \sigma_s^2/(1 - \theta^2)$. Defining $\rho_{st} = \boldsymbol{B(s)^t(\Sigma_\gamma + \Sigma_\nu + \mathbb{1}_{t>0}\Sigma_\Upsilon)B(s)}$, this implies a marginal predictive variance $\zeta_{st}^2 \equiv \rho_{st} + \lambda_s^2$ for size s at a new run i and a new UFP residual distribution p for random jump models. No-jump, jump, and random jump models define marginal

predictive variance ζ_{st}^2 equivalently, but no-jump and jump models remove $\boldsymbol{\Sigma_\Upsilon}$ from the definition of ρ_{st}. *Size bin means*, the back transformed mean of predicted counts for size bin s at time t, are then

$$\mu_{st} = \exp\bigl(\psi_{st} + \zeta_{st}^2/2\bigr). \tag{3.19}$$

Define s_t as the modal size bin at time t and the modal particle count as $h_t \equiv \operatorname{argmax}(\mu_{st})$, where the maximum is over size bins s for fixed t and μ_{st} is defined in (3.19).

For residual analysis, errors were initially calculated as

$$e_{ist} = y_{ist} - \bigl(\boldsymbol{\alpha}^T \boldsymbol{B}(s) + \boldsymbol{\gamma_i}^T \boldsymbol{B}(s) + \boldsymbol{f}(t)^T \boldsymbol{\Delta}_z \boldsymbol{B}(s) + \boldsymbol{g}(t)^T \boldsymbol{\Upsilon_i} \boldsymbol{B}(s)\bigr), \tag{3.20}$$

removing both fixed and run-specific random effects as implemented in Chaloner and Brant (1988), Chaloner (1994), and Weiss and Lazaro (1992). Minute-to-minute random effects and autoregressive error are not removed from equation (3.20) to better visualize lack of fit in the fixed and run-specific random effects that may be picked up by minute-to-minute size correlation $\boldsymbol{v_p}^T \boldsymbol{B}(s)$ and by the autoregressive term θ. The estimate for the autocorrelation term θ can be inflated if there is systematic lack of fit over size or time. Errors for no-jump and jump models are calculated omitting $\boldsymbol{g}(t)^T \boldsymbol{\Upsilon_i} \boldsymbol{B}(s)$ from the right-hand side of 3.20. Finally, we define errors $e_{ist}^* = e_{ist} - \boldsymbol{v_p}^T \boldsymbol{B}(s)$ to examine the variance not explained by minute-to-minute random effects.

4. Results. Figure 3 plots posterior means, $\bar{\mu}_{st} \equiv \mathrm{E}[\mu_{st}|Y]$, of windows open size bin means, μ_{st}, for no-jump, jump, and random jump models at $t = 5$, 15, and 20 minutes after the engine is turned on. Figure 3(d) plots posterior modal heights, $\hat{h}_t \equiv \operatorname{argmax}(\bar{\mu}_{st})$, as a function of t. The nonjump quadratic model predicts that counts will have an unintuitive sharp decrease between time $t = 15$ and $t = 20$; this decrease is not seen in the jump and random jump models. The jump appears to be a valuable addition to the model. Credible intervals are not plotted to ease visual interpretation, but there is overlap in these intervals for all models. Posterior estimates $\bar{\mu}_{st}$ and $\hat{h}_t$ for the windows closed position are more similar across all models over time, and these results are presented in Appendix A [Fischer et al. (2017)] in Figure A6.

Model choice was through a combination of DIC [Spiegelhalter et al. (2002)] and graphical examination of residuals. The model with the lowest DIC is the preferred model, however, other factors must also be taken into consideration during model selection. The DIC and components for each model are presented in Table 1.

Models were further evaluated by plotting mean posterior residuals, $\bar{e}_{ist} \equiv E[e_{ist}|\boldsymbol{Y}]$ as defined by equation (3.6), by time and by size. Figure 4 presents residuals $\bar{e}_{ist}$ for the quadratic, jump quadratic, and random jump models plotted against size and time. Adding the jump component to the model narrowed the range of mean posterior residuals and reduced outliers. Adding the random jump component reduced these to an even greater extent.

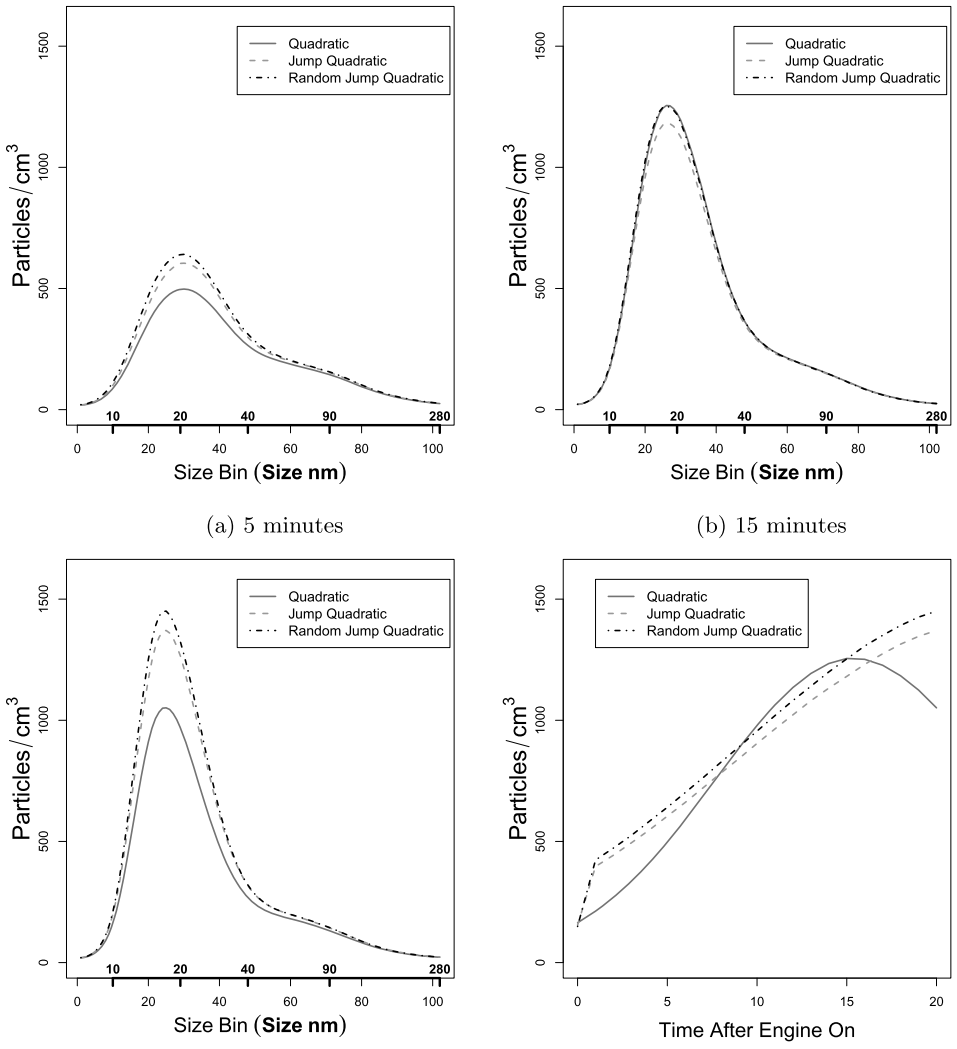

(a) 5 minutes

(b) 15 minutes

(c) 20 minutes

(d) Engine-On Modal Height

FIG. 3. *Posterior means,* $\bar{\mu}_{st} \equiv \mathrm{E}[\mu_{st}|Y]$*, of windows open size bin means,* μ_{st}*, for no-jump, jump, and random jump models at* (a) $t = 5$, (b) 15, *and* (c) 20 *minutes after the engine is turned on as well as the posterior modal heights,* $\hat{h}_t \equiv \mathrm{argmax}(\bar{\mu}_{st})$*, in* (d). *The nonjump quadratic model differs from knot models in that it predicts counts to sharply decrease from time* $t = 15$ *to* $t = 20$*, however, this decrease is removed with the addition of the jump. Credible intervals are not plotted to ease visual interpretation, but there is overlap in these intervals for all models.*

The posterior median $\hat{\theta}$ of the AR parameter for all models was about 0.06 with credible intervals of about $(0.05, 0.07)$, indicating this parameter was not sensitive to model choice.

TABLE 1
DIC calculations for models

Model	DIC	DIC bar	pD
Quadratic	−45,243.3	−47,740.0	2,496.7
Jump quadratic	−45,237.1	−47,738.1	2,501.0
Random jump quadratic	−45,283.4	−47,762.0	2,478.6

The random jump quadratic model had the best (lowest) DIC score. Of all the models, it also had superior fit when looking at the residuals not adjusted for minute-to-minute random effects or AR. The fit of the model at engine-off was also vastly improved. Plots showing the improvement in fit are presented in Appendix A [Fischer et al. (2017)] in Figures A7 and A8. The random jump quadratic model was selected to present further inferences.

Minute-to-minute random effects $\boldsymbol{v}_p^T \boldsymbol{B}(s)$ did a great deal to further explain correlation in residual variance over size, as residuals $\bar{e}^*_{ist} \equiv E[e^*_{ist}|\boldsymbol{Y}]$ demonstrate in Figure 5(a) and (b). Residual variance shows slight heteroskedasticity over size bin, with smaller sizes showing higher variances. Figure 5(c) plots posterior median and 95 percent credible intervals for σ_s^2 by bin size.

Figure 6 plots baseline posterior mean log counts by size bin for $t < 0$ for all runs i. The plots show significant variation in baseline UFP size distributions across run.

B-splines in the model above used seven equally spaced knots. As a sensitivity analysis, we experimented with alternate numbers of equally spaced knots to determine the effect on inference and model fit. Choosing seven knots resulted in a superior DIC score and much lower posterior median estimate for the AR parameter θ compared to models with fewer knots. Using eight or nine equally spaced knots did result in lower DIC scores, but the posterior median estimates for θ were unchanged and these additional knots had little effect on model inferences. Because these higher knot models also resulted in significantly greater computing requirements, seven knots was chosen as a sensible compromise. DIC scores, AR estimates, and model inferences for alternate knot choices are presented in Appendix A [Fischer et al. (2017)] in Section A.5 and Figures A9 and A10.

To determine the sensitivity of model inference to prior choice, we also fit models halving and doubling prior variances for the fixed effects and prior mean variances for the random effects, which were given priors to utilize information across runs from the data. Results were invariant to changes in prior variances for the fixed effects and the minute-to-minute and jump random effects. Changes to the prior mean for engine-off random effects, which used substantive prior information available from other experiments not used in these analyses, did result in some changes in inference: halving this variance resulted in an approximate 10 percent reduction in posterior estimates for $\bar{\mu}_{st}$, while doubling it resulted in about a 10

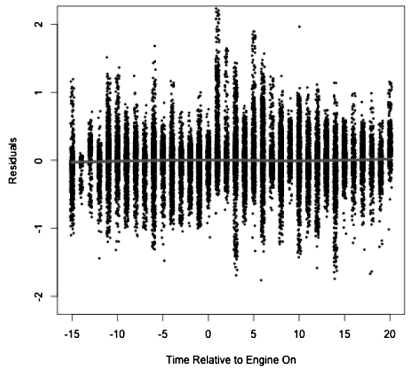

(a) Nonjump Quadratic $\bar{e}_{ist}$ Over Time

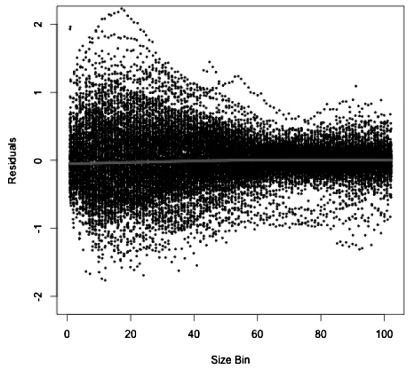

(b) Nonjump Quadratic $\bar{e}_{ist}$ Residuals Over Size

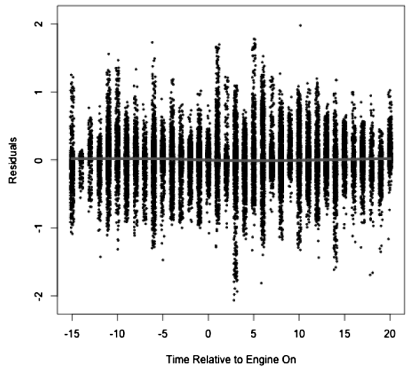

(c) Jump Quadratic $\bar{e}_{ist}$ Over Time

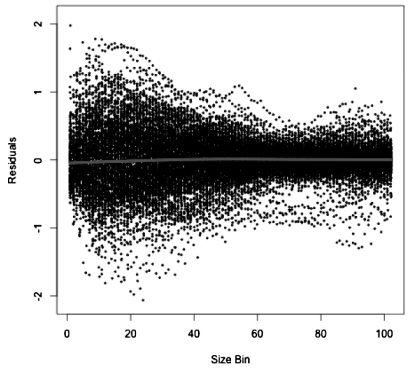

(d) Jump Quadratic $\bar{e}_{ist}$ Over Size

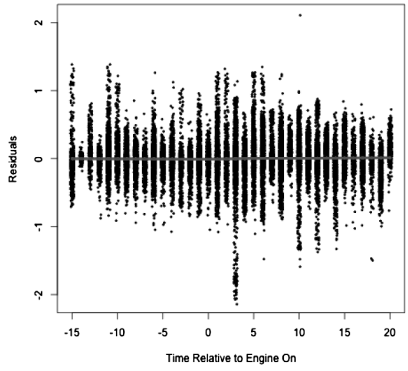

(e) Random Jump Quadratic Over Time

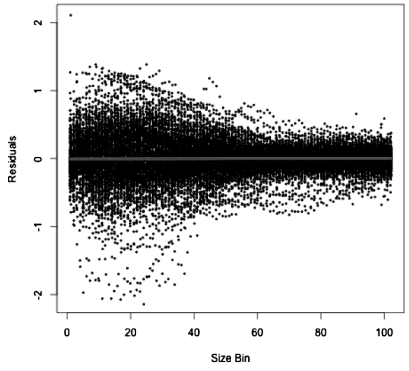

(f) Random Jump Quadratic Over Size

FIG. 4. *Residuals $\bar{e}_{ist}$ for the quadratic, jump quadratic, and random jump models plotted against time and size bin. Adding the jump component to the model narrowed the range of mean posterior residuals and reduced outliers. Adding the random jump component reduced these to an even greater extent.*

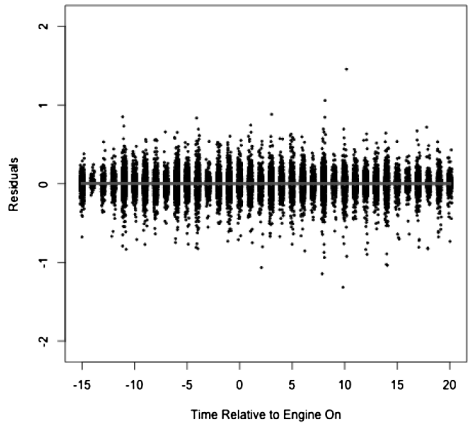

(a) Residuals $\bar{e}^*_{ist}$ Over Time

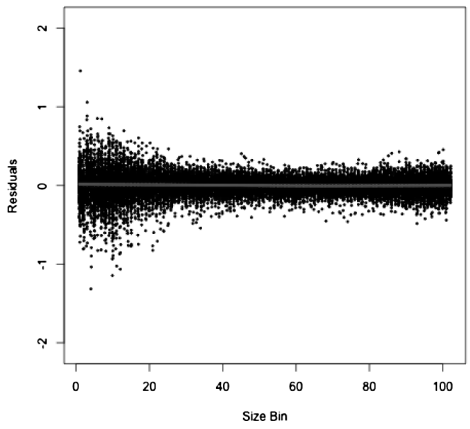

(b) Residuals $\bar{e}^*_{ist}$ Over Size

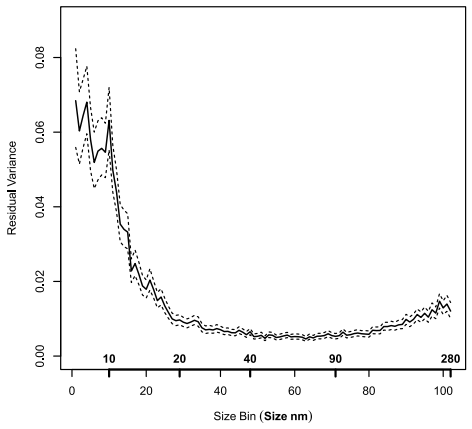

(c) σ_s^2 as a Function of Size Bin

FIG. 5. *Residuals $\bar{e}^*_{ist}$ for the random jump model plotted against time in Figure* (a) *and size bin in Figure* (b). *Minute-to-minute random effects $\boldsymbol{v}_p^T \boldsymbol{B}(s)$ did a great deal to further explain correlation in residual variance over size. Residual variance shows slight heteroskedasticity over size bin. Figure* (c) *shows posterior medians and* 95 *percent credible intervals for σ_s^2 as a function of size bin.*

percent increase in estimates. This is to be expected given only $R = 21$ runs, where an informative prior using information from other experiments provides valuable additional information not available in the data. Results from this sensitivity analysis are also presented in Appendix A [Fischer et al. (2017)] in Section A.6 and Figures A11 and A12.

Time trend components are presented at $t = 15$ in Figure 7. Figure 7(a) plots posterior means of the jump component, $\mathrm{E}[\boldsymbol{\Delta}_{z1}^T \boldsymbol{B}(s)|Y]$, (b) plots posterior means of 15 times the linear component, $\mathrm{E}[15 * \boldsymbol{\Delta}_{z2}^T \boldsymbol{B}(s)|Y]$, and (c) plots posterior means

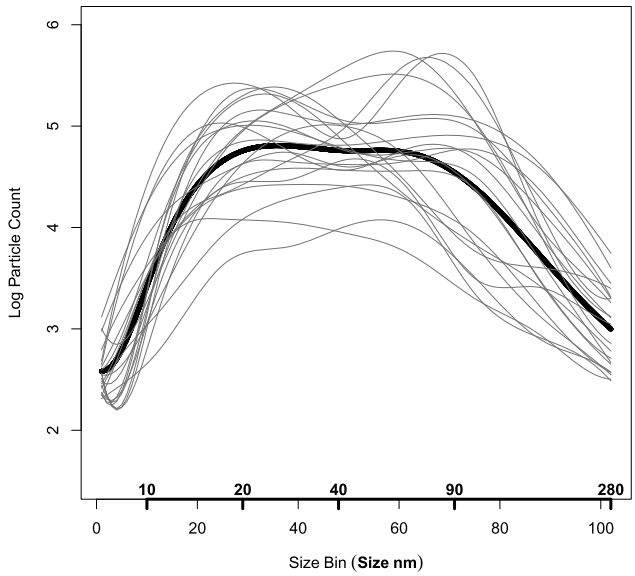

FIG. 6. *Posterior mean log baseline counts by size bin for $t < 0$. The thick black curve is the posterior population mean, and the lighter curves show posterior mean log counts by size bin for individual run i.*

of 15^2 times the quadratic component, $\mathrm{E}[15^2 \boldsymbol{\Delta}_{z3}^{\boldsymbol{T}} \boldsymbol{B}(\boldsymbol{s})|Y]$, for both window positions. Adding these curves together gives the net log particle count increase after 15 minutes with the engine-on. The jump component is negligible for the windows closed position, but there is an initial jump estimated for the windows open position for all size bins, with the greatest increase for particles between 10 and 40 nm. For particle sizes between 10 and 90 nm, the linear component is larger for the windows open position than the windows closed position. Negative values across size bin for both windows positions in the quadratic component imply that particle counts increase at slower rates for all bins as the engine continues to run, though these rate decreases are smaller across size for the windows closed position. Credible intervals are not plotted, as there is overlap across all size bins, however, Figure (d) plots posterior means for the difference in jump, linear, and quadratic components for windows open minus windows closed to show for all components there is a nonzero difference between the two scenarios for most size bins at $t = 15$. Ninety-five percent credible intervals are plotted with thin lines.

In Figure 8, $\bar{\mu}_{st}$ are plotted against s for engine-off and for windows open and closed after the engine has been idling for (a) 5, (b) 10, (c) 15, and (d) 20 minutes for the random jump quadratic model. Adding the random jump both increased predicted means and widened credible intervals compared to models without it. The windows open position has higher predicted counts for sizes between about 15 and 30 nm at all time points except $t = 20$ compared to the windows closed

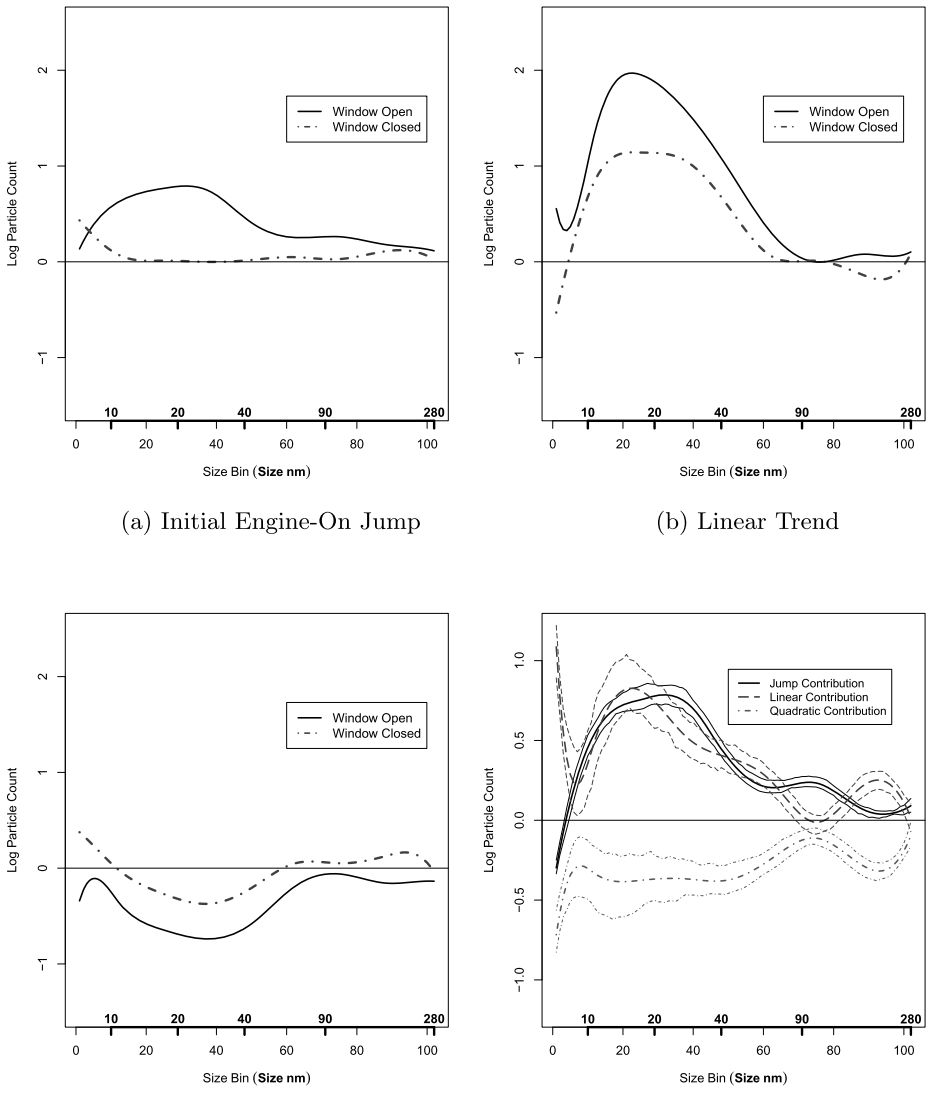

(a) Initial Engine-On Jump

(b) Linear Trend

(c) Quadratic Trend

(d) Window Open/Closed Differences

FIG. 7. *Posterior fixed time trend components on the log scale. Figure* (a) *plots the jump component*, $\mathrm{E}[\boldsymbol{\Delta}_{z1}^{T}\boldsymbol{B}(s)|Y]$, (b) *plots the linear component*, $\mathrm{E}[15 * \boldsymbol{\Delta}_{z2}^{T}\boldsymbol{B}(s)|Y]$, *and* (c) *plots the quadratic component* $\mathrm{E}[15^2\boldsymbol{\Delta}_{z3}^{T}\boldsymbol{B}(s)|Y]$ *for both window positions. Adding these curves together gives the net log particle count increase after* 15 *minutes. The jump component is negligible for the windows closed position, but there is an initial jump estimated for the windows open position for all size bins. The linear component is larger for the windows open position than the windows closed position for most size bins. Negative values across size bin for both window positions in the quadratic component imply that particle counts increase at slower rates for all bins as the engine continues to run. Figure* (d) *plots posterior means for the difference in jump, linear, and quadratic contributions for windows open vs. windows closed to show there is a nonzero difference between the two scenarios at* $t = 15$ *for most size bins. Ninety-five percent credible intervals are plotted with thin lines.*

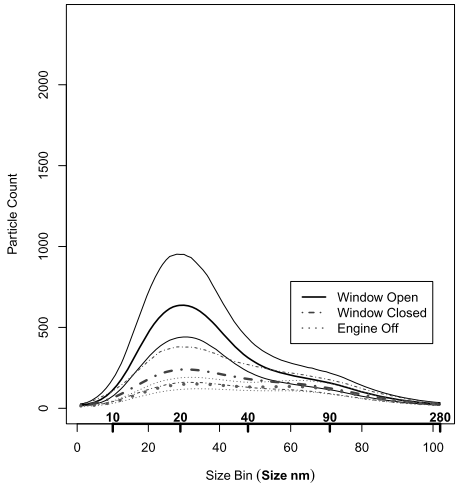

(a) Idling 5 Minutes

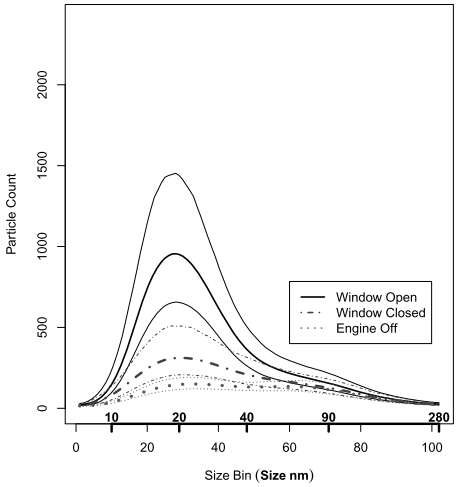

(b) Idling 10 Minutes

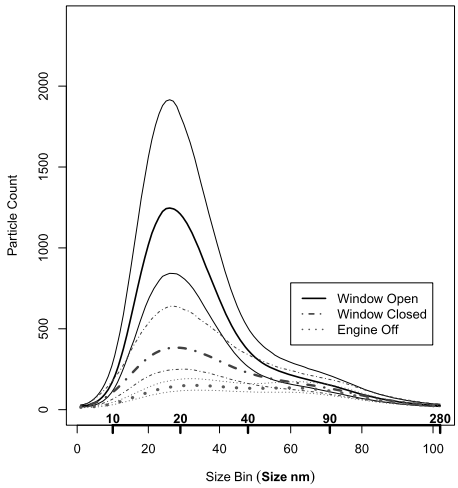

(c) Idling 15 Minutes

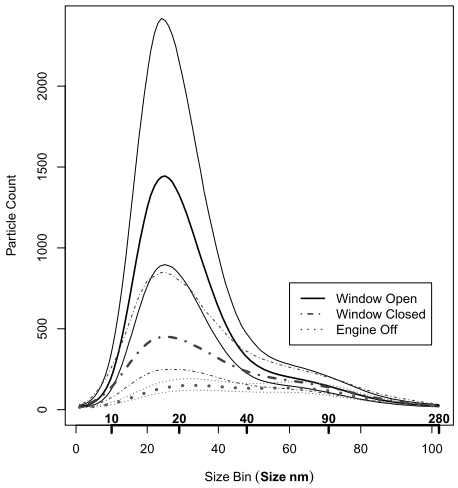

(d) Idling 20 Minutes

FIG. 8. *Posterior means, $\bar{\mu}_{st}$, of size bin means for engine-off are plotted in all figures. Windows open and closed posterior means are plotted after the engine has been idling for* (a) 5, (b) 10, (c) 15, *and* (d) 20 *minutes for the random jump quadratic model. Thin lines are* 95 *percent credible intervals. Adding the random jump both increased predicted means and widened credible intervals. The windows open position has higher predicted counts for sizes between about* 15 *and* 30 *nm at all time points except for $t = 20$ compared to the windows closed position, and also becomes much more peaked over time as the mode gets higher and higher. The windows closed position predictions increase over time at a slower, more constant rate.*

position, and also becomes much more peaked over time as its mode gets higher and higher. The windows closed position predictions increase over time at a slower, more constant rate. While before 10 minutes credible intervals between the engine-off and windows closed curves overlap slightly, at 10 minutes particles of sizes less than 30 nm show increases from the engine-off state which increase further at 15 minutes. Closing windows hinders self-pollution over time but does not prevent it.

Figure 9 plots posterior medians, $\hat{s}_t$, of mode locations, s_t, and posterior modal heights, $\hat{h}_t$, defined previously. The location of the mode in the engine-off state is uncertain, with 95 percent credible intervals $(33, 64)$, equivalent to a size range of 23–71 nm (full credible interval not shown on plot). In 9(a), the windows open mode location decreases in size, and the credible interval rapidly narrows to finally reach $(23, 27)$ at 20 minutes. The windows closed position mode location in 9(b) decreases at a slower rate and with more uncertainty: at 20 minutes the 95 percent credible interval is $(21, 36)$. In Figure (c), $\hat{h}_t$ reach counts of over 1400 for windows open at $t = 20$ compared to about 450 for windows closed. The windows closed position has posterior mode heights that increase at an almost linear rate over time that is slower than for the windows open position. Credible intervals do not overlap, but get wider over time for both window positions.

In Appendix A [Fischer et al. (2017)], Section A7, we present results from a simulation study with parameters set to the posterior means from the final model and find that posterior mean estimates are consistent with the truth and that coverage is generally acceptable.

5. Discussion. Our use of mixed-model functional time-series methods greatly reduce the size of confidence intervals compared to the nonfunctional univariate longitudinal methods used in Zhang et al. (2012) which show overlap for both window positions at all size bins. Our methods permit inference about actual particle counts not available using modal methods. Though estimates for residual variance over size were small in this dataset, in other cases error can be much higher for smaller size bins so that having this component in the model is very beneficial [Ramsay and Silverman (2005)].

At all time points the windows open position had higher predictions for particles between about 15 and 22 nm than windows closed, but predictions for the windows closed position continued to increase over time. Having the window closed does not prevent UFPs from entering the bus cabin, particularly for particles less than 22 nm.

A major benefit of these methods are the ease in which model fit can be evaluated, both through the use of DIC and through residual checks allowing visual inspection of model fit across size bin and time. Graphical techniques also allow for the evaluation of the fit of random effects. Plots demonstrating a subset of these residual checks for random effects are included in the Supplementary Material [Fischer et al. (2017)]. Our methods are easily adapted to different model

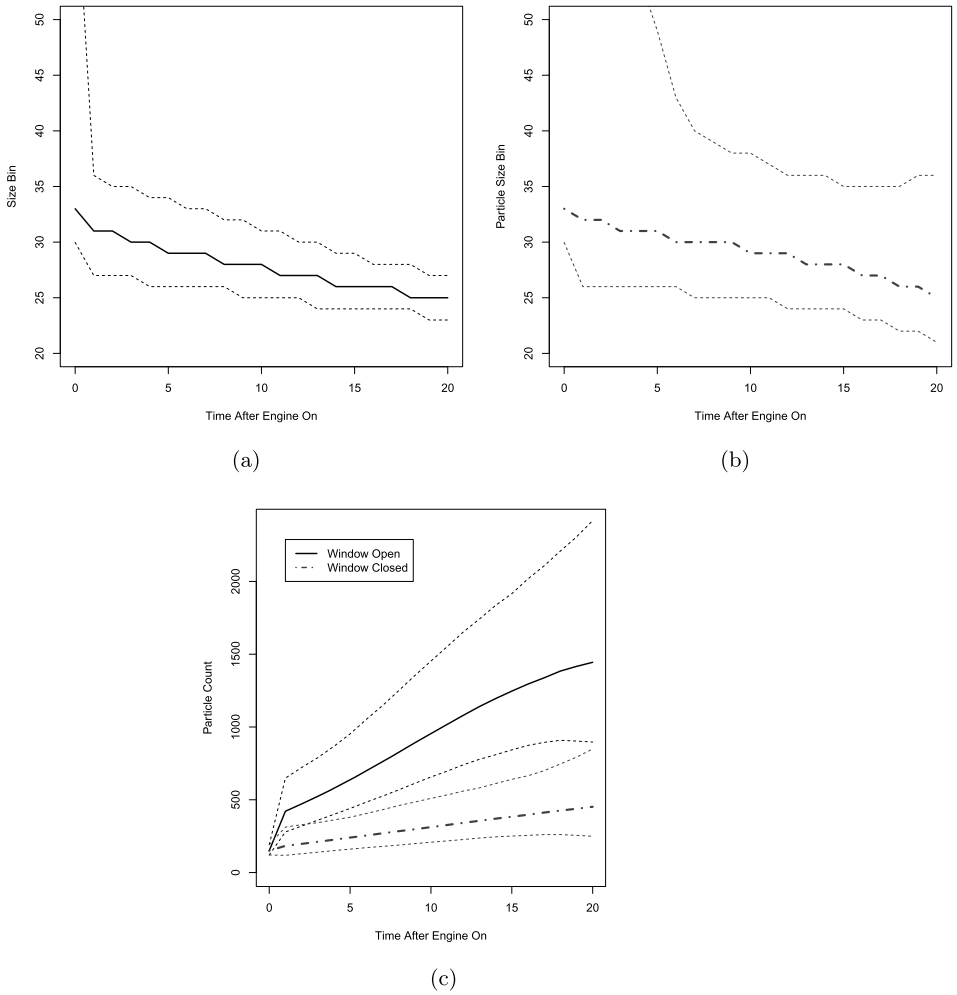

FIG. 9. *Median posterior mode locations,* $\hat{s}_t$*, for* (a) *windows open and* (b) *windows closed, and* (c) *posterior modal heights,* $\hat{h}_t$*, over time for both window positions with* 95 *percent credible intervals. The location of the mode in the engine-off state is uncertain, with* 95 *percent credible intervals* (33, 64)*, equivalent to a size range of* 23–71 *nm (full credible interval not shown on plot). In Figure* (a)*, the windows open mode location rapidly narrows, while in* (b) *the windows closed position mode location decreases at a slower rate and with more uncertainty. Posterior mode heights* $\hat{h}_t$ *in Figure* (c) *for the windows closed position increase at a slower, almost constant linear rate over time. Credible intervals do not overlap, but get wider over time for both window positions.*

specifications, such as a different form for the time trends or engine-on random effects and other variance structures.

Our methods allow uncertainty in predictions to be quantified and communicated graphically in ways easily interpretable to a nonstatistician. We provide sta-

tistical summaries of useful quantities currently used by researchers such as mode locations and heights.

A limitation of the current methods is that they do not take into account other factors that may affect particle distribution such as engine type, organic content of diesel fuel, engine load, and the conditions of combustion. Thus, current conclusions cannot be generalized to all conditions. This is a valuable direction for future research.

Our methods provide a basis to monitor exposure to UFPs based on particle counts separated into particles of different groups of size bins. These methods provide information needed for understanding vehicle emissions' contribution to UFP counts. Our methods allow evaluation and comparison of emissions by particle size for UFPs.

SUPPLEMENTARY MATERIAL

Appendix A: Online supplementary material (DOI: 10.1214/16-AOAS1004SUPPA; .zip). Supplementary analyses referred to in manuscript.

Appendix B: Dataset and source code (DOI: 10.1214/16-AOAS1004SUPPB; .zip). R and JAGS programs to perform analyses and produce plots and original dataset.

REFERENCES

ALESSANDRINI, F., SCHULZ, H., TAKENAKA, S., LENTNER, B., KARG, E., BEHRENDT, H. and JAKOB, T. (2006). Effects of ultrafine carbon particle inhalation on allergic inflammation of the lung. *Journal of Allergy and Clinical Immunology* **117** 824–830.

BALADANDAYUTHAPANI, V., MALLICK, B. K. and CARROLL, R. J. (2005). Spatially adaptive Bayesian penalized regression splines (P-splines). *J. Comput. Graph. Statist.* **14** 378–394. MR2160820

BENNETT, W. D. and ZEMAN, K. L. (1998). Deposition of fine particles in children spontaneously breathing at rest. *Inhalation Toxicology* **10** 831–842.

BERHANE, K. and MOLITOR, N. T. (2008). A Bayesian approach to functional-based multilevel modeling of longitudinal data: Applications to environmental epidemiology. *Biostatistics* **4** 686–699.

CHALONER, K. (1994). Residual analysis and outliers in Bayesian hierarchical models. In *Aspects of Uncertainty*. 149–157. Wiley, Chichester. MR1309691

CHALONER, K. and BRANT, R. (1988). A Bayesian approach to outlier detection and residual analysis. *Biometrika* **75** 651–659.

CRAINICEANU, C. M., RUPPERT, D., CARROLL, R. J., JOSHI, A. and GOODNER, B. (2007). Spatially adaptive Bayesian penalized splines with heteroscedastic errors. *J. Comput. Graph. Statist.* **16** 265–288. MR2370943

DE BOOR, C. (1978). *A Practical Guide to Splines*. *Applied Mathematical Sciences* **27**. Springer, New York. MR0507062

DELFINO, R. J., SIOUTAS, C. and MALIK, S. (2005). Potential role of ultrafine particles in associations between airborne particle mass and cardiovascular health. *Environmental Health Perspectives* **113** 934–946.

EPA (2002). Health assessment document for diesel engine exhaust. The National Technical Information Service, Springfield, VA.

EPA (2014). Clean school bus USA. Available at http://www.epa.gov/cleanschoolbus/csb-overview.htm.

FERIN, J., OBERDORSTER, G., PENNEY, D. P., SODERHOLM, S. C., GELEIN, R. and PIPER, H. C. (1990). Increased pulmonary toxicity of ultrafine particles? *Journal of Aerosol Science* **21** 384–387.

FISCHER, H. J, ZHANG, Q., ZHU, Y. and WEISS, R. E (2017). Supplement to "Functional time series models for ultrafine particle distributions." DOI:10.1214/16-AOAS1004SUPPA, DOI:10.1214/16-AOAS1004SUPPB.

FRAMPTON, M. W., STEWART, J. C., OBERDORSTER, G., MORROW, P. E., CHALUPA, D., PIETROPAOLI, A. P., FRASIER, L. M., SPEERS, D. M., COX, C., HUANG, L. S. and UTELL, M. J. (2006). Inhalation of ultrafine particles alters blood leukocyte expression of adhesion molecules in humans. *Environmental Health Perspectives* **114** 51–58.

GELFAND, A. E. and SMITH, A. F. M. (1990). Sampling-based approaches to calculating marginal densities. *J. Amer. Statist. Assoc.* **85** 398–409. MR1141740

GOLDSMITH, J. and KITAGO, K. (2013). Assessing systematic effects of stroke on motor control using hierarchical scalar-on-function regression. Techical report, Columbia Univ., New York, NY.

HADFIELD, J. D. (2010). MCMC methods for multi-response generalized linear mixed models: The MCMCglmm R package. *J. Stat. Softw.* **33** 1–22.

HASTIE, T. and TIBSHIRANI, R. (1993). Varying-coefficient models. *J. R. Stat. Soc. Ser. B. Stat. Methodol.* **55** 757–796. MR1229881

HASTINGS, W. K. (1970). Monte Carlo sampling methods using Markov chains and their applications. *Biometrika* **57** 97–109.

HUSSEIN, T., MASO, M. D., PETÄJÄ, T., KOPONEN, I. K., PAATERO, P., AALTO, P., HÄMERI, K. and KULMALA, M. (2005). Evaluation of an automatic algorithm for fitting the particle number size distributions. *Boreal Environment Research* **10** 337–355.

LANG, S. and BREZGER, A. (2004). Bayesian P-splines. *J. Comput. Graph. Statist.* **13** 183–212. MR2044877

MORAWSKA, L., RISTOVSKI, Z., JAYARATNE, E. R., KEOGH, D. U. and LING, X. (2008). Ambient nano and ultrafine particles from motor vehicle emissions: Characteristics, ambient processing and implications on human exposure. *Atmospheric Environment* **42** 8113–8138.

MORRIS, J. (2015). Functional regression. *Annual Review of Statistics and Its Application* **2** 321–359.

MORRIS, J. S., VANNUCCI, M., BROWN, P. J. and CARROLL, R. J. (2003). Wavelet-based nonparametric modeling of hierarchical functions in colon carcinogenesis. *J. Amer. Statist. Assoc.* **98** 573–597. MR2011673

OBERDORSTER, G., SHARP, Z., ATUDOREI, V., ELDER, A., GELEIN, R., KREYLING, W. and COX, C. (2004). Translocation of inhaled ultrafine particles to the brain. *Inhalation Toxicology* **16** 437–445.

PALMER, J. and PETTIT, L. (1996). Risks of using improper priors with Gibbs sampling and autocorrelated errors. *J. Comput. Graph. Statist.* **5** 245–249.

PLUMMER, M. (2003). JAGS: A program for analysis of Bayesian graphical models using Gibbs sampling In *Proceedings of the 3rd International Workshop on Distributed Statistical Computing*, Vienna.

PRADO, R. and WEST, M. (2010). *Time Series*: *Modeling*, *Computation*, *and Inference*. CRC Press, Boca Raton, FL.

RAMSAY, J. O. and SILVERMAN, B. W. (2005). *Functional Data Analysis*, 2nd ed. Springer, New York.

SAMET, J. M., RAPPOLD, A., GRAFF, D., CASCIO, W. E., BERNTSEN, J. H., HUANG, Y. C. T., HERBST, M., BASSETT, M., MONTILLA, T., HAZUCHA, M. J., BROMBERG, P. A. and DEVLIN, R. B. (2009). Concentrated ambient ultrafine particle exposure induces cardiac changes in young healthy volunteers. *American Journal of Respiratory and Critical Care Medicine* **179** 1034–1042.

SPIEGELHALTER, D. J., BEST, N. G., CARLIN, B. P. and VAN DER LINDE, A. (2002). Bayesian measures of model complexity and fit. *J. R. Stat. Soc. Ser. B. Stat. Methodol.* **64** 583–639. MR1979380

WEISS, R. E. and LAZARO, C. G. (1992). Residual plots for repeated measures. *Stat. Med.* **11** 115–124.

WHITBY, P. H. (1978). Modal aerosol dynamics modelling. Technical report, U.S. Environment Protection Agency, Atmospheric Research and Exposure Assessment Laboratory, Washington, DC.

WHITBY, P. H., MCMURRY, P. H., SHANKER, U. and BINKOWSKI, F. S. (1991). Modal aerosol dynamics modeling. Technical report, U.S. Environment Protection Agency, Atmospheric Research and Exposure Assessment Laboratory, Washington, DC.

WRAITH, D., ALSTON, C., MENGERSEN, K. and HUSSEIN, T. (2009). Bayesian mixture model estimation of aerosol particle size distributions. *Environmetrics* **22** 23–34.

WRAITH, D., MENGERSEN, K., ALSTON, C., ROUSSEU, J. and HUSSEIN, T. (2014). Using informative priors in the estimation of mixtures over time with application to aerosol particle size distributions. *Ann. Appl. Stat.* **8** 232–258. MR3191989

ZHANG, Q., FISCHER, H. J., WEISS, R. E. and ZHU, Y. (2012). Ultrafine particle concentrations in and around idling school buses. *Atmospheric Environment* **69** 65–75.

H. J. FISCHER
DEPARTMENT OF RESEARCH AND EVALUATION
KAISER PERMANENTE SOUTHERN CALIFORNIA
100 S. LOS ROBLES AVE.
PASADENA, CALIFORNIA 91101
USA
E-MAIL: heidi.fischer@kp.org

R. E. WEISS
DEPARTMENT OF BIOSTATISTICS
FIELDING SCHOOL OF PUBLIC HEALTH
UNIVERSITY OF CALIFORNIA, LOS ANGELES
LOS ANGELES, CALIFORNIA 90095-1772
USA
E-MAIL: robweiss@ucla.edu

Q. ZHANG
Y. ZHU
DEPARTMENT OF ENVIRONMENTAL HEALTH SCIENCES
UCLA FIELDING SCHOOL OF PUBLIC HEALTH
LOS ANGELES, CALIFORNIA 90095-1772
USA
E-MAIL: zhangqunfang@gmail.com
yifang@ucla.edu